International Journal of Refrigeration 176 (2025) 66–78

Contents lists available at ScienceDirect

International Journal of Refrigeration

journal homepage: www.elsevier.com/locate/ijrefrig

INSTITUT INTERNATIONAL DU FROID
INTERNATIONAL INSTITUTE OF REFRIGERATION

Coconut shell derived activated carbon for effective separation of greenhouse gases

Julio E. Sosa, Rui.P.P.L. Ribeiro [1], Inês Matos, Maria Bernardo, Isabel M. Fonseca, José P.B. Mota, João M.M. Araújo, Ana B. Pereiro [*]

LAQV, REQUIMTE, Department of Chemistry, NOVA School of Science and Technology, NOVA University Lisbon, 2829-516 Caparica, Portugal

ARTICLE INFO

Keywords:
Adsorption
F-gases
Gas separation
GHGs
Porous materials
Refrigerants

ABSTRACT

The development of efficient adsorbent materials for the selective capture of greenhouse gases (GHGs) is crucial. The porosity and surface area of the materials are key factors for the GHGs separation. This study demonstrates how waste from coconut shell (CS) biomass can be used to design novel biomaterials (CS-CO_2, CS-$ZnCl_2$) with enhanced GHG selectivity. A comparison with activated carbon monoliths (ACM) and a metal-organic framework (Fe-BTC) was carried out to assess the impact of different porous matrices on GHGs capture. The adsorption equilibrium of R-32, R-125, R-134a, R-143a, CO_2, and CH_4 on these materials was measured between 283.15–323.15 K. The adsorption isotherms obtained were fitted using the dual-site Langmuir model. For R-32, R-125, R-134a and R-143a, the adsorption capacity follows ACM > CS-$ZnCl_2$ > Fe-BTC > CS-CO_2 due to the decrease of the surface area. The CO_2 adsorption capacity is ACM > Fe-BTC > CS-$ZnCl_2$ > CS-CO_2, which is related to the micropore volume. In this case, CS-CO_2 has a smaller adsorption capacity but is similar to ACM and outperforms Fe-BTC at $P < 0.4$ MPa. The selectivity of R-410A, R-407C, R-404A, and CO_2/CH_4 blends was determined with the Ideal Adsorbed Solution Theory (IAST). CS-$ZnCl_2$ shows a higher selectivity for R-125 over R-32 in R-410A and R-407C separations due to its larger pore volume. CS-CO_2 predominantly adsorbs R-134a and R-143a over R-125 in R-404A separation. ACM preferentially adsorbs CO_2 over CH_4 due to its large, elongated micropores. This study introduces innovative materials that improve GHGs separation and help reduce emissions.

1. Introduction

Climate change is an undeniable reality. The Earth's average temperature is rising by approximately 1.5–2 °C, resulting in more frequent and severe extreme weather events (Beans, 2023; Díaz Tautiva et al., 2024). This phenomenon affects developed and developing countries worldwide, driven primarily by the exponential increase in greenhouse gas (GHG) emissions (Díaz Tautiva et al., 2024; Tauseef Hassan et al., 2024). While developing countries contribute less to global emissions, they are disproportionately impacted by the consequences. These effects are particularly harsh due to their economic vulnerability, limited infrastructure, and heavy reliance on climate-sensitive sectors such as agriculture and fisheries (Andreoni A, 2024; Bolan et al., 2024; Flores et al., 2024; Pizzorni et al., 2024). Rising temperatures and shifting precipitation patterns reduce agricultural productivity, leading to food shortages and rising prices. Additionally, prolonged droughts and melting glaciers exacerbate water scarcity, further threatening livelihoods. Poor air quality, a direct result of GHGs emissions, contributes to respiratory diseases that disproportionately affect vulnerable populations (Andreoni A, 2024; Flores et al., 2024; Pizzorni et al., 2024). A key factor is also the growing demand for food and services due to the exponential growth of the human population (Díaz Tautiva et al., 2024; Tauseef Hassan et al., 2024). Additionally, deforestation, increased chemical usage in industrial processes and agricultural activities, and the poor maintenance and management of equipment at the end of its life cycle must also be considered.

In 2022, GHG emissions consisted of 71.6 % CO_2, 21 % CH_4, 4.8 % N_2O, and 2.6 % fluorinated gases (F-gases) (European Commission, 2019; Gonzalez-Olmos and Llovell, 2024; Miranda et al., 2023; Publications Office of the European Union, 2023; Schulz and Kourkoulas, 2014; Vollmer et al., 2015). These GHGs are commonly used in various industrial processes. For example, CO_2 is used in the oil industry for hydraulic fracturing (Abdelaziz O, 2023). This technology facilitates the extraction of CH_4 from underground shale gas reserves and the geological storage of CO_2 (Russell et al., 2020; Shen et al., 2024).

* Corresponding author.
E-mail address: anab@fct.unl.pt (A.B. Pereiro).
[1] Current Address: HyLab - Green Hydrogen Collaborative Laboratory, Estrada Nacional 120-1 Central Termoeléctrica, 7520-089 Sines, Portugal.

https://doi.org/10.1016/j.ijrefrig.2025.04.022
Received 19 January 2025; Received in revised form 23 April 2025; Accepted 24 April 2025
Available online 25 April 2025

Nomenclature

Acronyms

ACM	Activated carbon monoliths
Bio-Acs	Biomaterials
C	Carbon
CH_4	Methane
CO_2	Carbon dioxide
CS	Coconut shell
DFT	Density functional theory
EA	Elemental analysis
F-gases	Fluorinated gases
FTIR	Fourier-transform infrared spectroscopy
GHGs	Greenhouse gases
GWP	Global warming potential
H	Hydrogen
MOF	Metal-Organic Framework
N	Nitrogen
NIST	National Institute of Standards and Technology
R-125	Pentafluoroethane
R-134a	1,1,1,1-tetrafluoroethane
R-143a	1,1,1,1-trifluoroethane
R-32	Difluoromethane
S	Sulphur
TFA	Trifluoroacetic acid
TGA	Thermal gravimetric analysis
VSA	Vacuum swing adsorption

Roman symbols

A	Virial coefficient
B	Virial coefficient
b_{12}	Adsorption affinity
C	Virial coefficients
K_H	Henry's constant
m_h	Mass of the measuring cell (g)
m_s	Mass of the porous solid matrix (g)
N_{exp}	Number of experimental points
P	Pressure (MPa)
q	Absolute adsorbed amount (mmol g^{-1})
q_{ex}	Amount adsorbed in excess (mmol g^{-1})
q_{exp}	Experimental amount adsorbed (mmol g^{-1})
q_{fit}	Adjusted adsorbed quantity (mmol g^{-1})
$q_{m1,2}$	Maximum amount of adsorption (mmol g^{-1})
R_g	Ideal gas constant (J K^{-1} mol^{-1})
S	Selectivity
S_{BET}	Surface area (m^2 g^{-1})
T	Temperature (K)
V_h	Volume of the measuring cell (cm^3)
v_{meso}	Mesopore volume (cm^3 g^{-1})
v_{micro}	Micropore volume (cm^3 g^{-1})
V_P	Specific volume of the adsorbent (cm^3 g^{-1})
v_{total}	Total pore volume (cm^3 g^{-1})
w	Apparent mass (g)
x	Mole fraction adsorbed of the gas by the adsorbent
y	Mole fraction of gas in the gas phase

Greek symbols

ΔH	Isosteric heat of adsorption (J mol^{-1})
ρ_g	Density of the gas (g cm^{-3})

Subscripts

exp	Experimental
fit	Adjusted
g	Gas

However, during the process of extracting CH_4, it is susceptible to CO_2 contamination. On the other hand, biogas has gained significant attention as a potential energy source due to its ease of production. However, the current production method yields a mixture of 40–60 % CH_4, 30–40 % CO_2, and other gases (N_2, O_2, H_2S, CO, NH_3, and siloxanes). Therefore, a purification process is necessary before this gas can be used as an

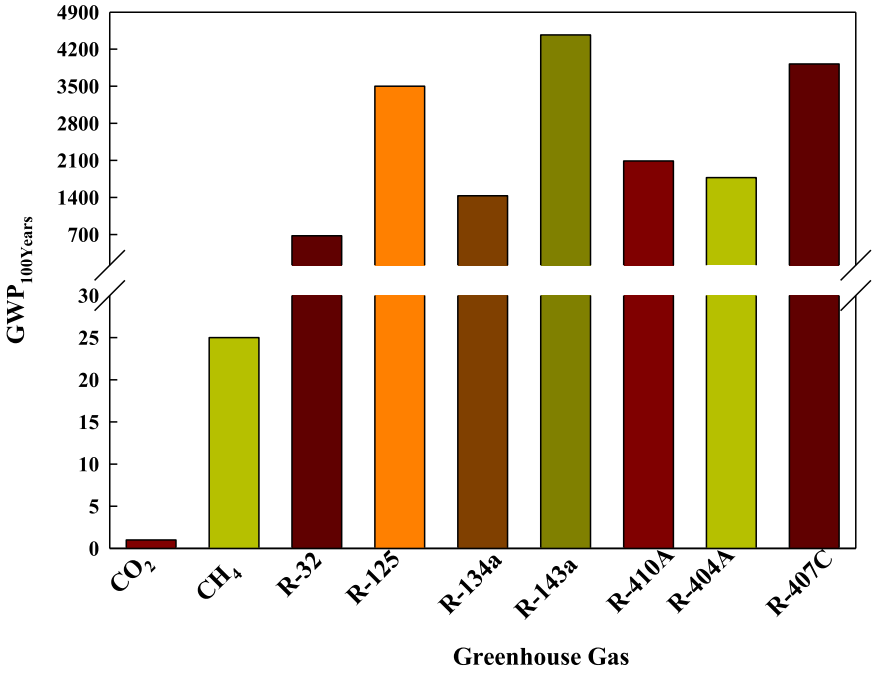

Fig. 1. The global warming potential of the greenhouse gases studied in this work (Abdelaziz O, 2023; Durkee, 2006).

energy source (Abd et al., 2023; Ferreira et al., 2021; Hossain et al., 2024; Ryckebosch et al., 2011; Staudt et al., 2024; Surra et al., 2022).

Fluorinated gases (F-gases) are commonly used in the refrigeration industry for food transport, industrial air conditioning, commercial air conditioning, and automotive air conditioning (Isler-Kaya and Karaosmanoglu, 2023). F-gases can be used in equipment either as pure gases or as mixtures (refrigerant blends), depending on their cooling capacity. The most commonly used pure F-gases in the European market are R-32, R-125, R-134a, and R-143a, while the most common blends are R-410A, R-407C, and R-404A (Cardoso et al., 2017; Islam and Saha, 2024a, 2024b; Isler-Kaya and Karaosmanoglu, 2023; Mota-Babiloni et al., 2017). Although these F-gases are widely used in the refrigeration industry worldwide, Fig. 1 demonstrates that they have a higher global warming potential (GWP) than other GHGs (Abdelaziz O, 2023). Additionally, F-gases are released into the atmosphere based on equipment maintenance or the disposal practices of equipment at the end of their life cycle. Finally, F-gases can decompose in the atmosphere, forming trifluoroacetic acid (TFA) (Henne et al., 2012; Holland et al., 2021; Jordan and Frank, 1999; Solomon et al., 2016; Wang et al., 2018). TFA is highly soluble in water, precipitates in the soil, and bioaccumulates in water sources (Holland et al., 2021; Jordan and Frank, 1999; Solomon et al., 2016). High TFA concentrations can increase water acidity and cause irritation of the nasal passages of mammals (Ball and Wellington, 1993; da Costa et al., 2021; Henne et al., 2012; Holland et al., 2021; Jordan and Frank, 1999; Solomon et al., 2016).

Reducing GHG emissions is a global priority, and the development of technology to separate, capture, and prevent the release of GHGs into the atmosphere is crucial. This effort requires continuous improvement and optimization, considering the current global context. In this work, the developed technology focuses on GHG adsorption on porous solid matrices such as metal-organic frameworks (MOFs), activated carbons (ACs), and biomaterials (Bio-ACs) is evaluated. These porous solid matrices possess diverse structural characteristics, including surface area, microporosity, mesoporosity and surface functional groups, which play a vital role in the adsorption of GHGs.

In the field of porous solid matrices, MOFs are thermally stable, have a good surface area and have structural flexibility (Nath et al., 2024; Obi et al., 2024; Surya Babu et al., 2024; Zeng et al., 2024). The literature demonstrates that CO_2 is selectively adsorbed on MOFs due to the interactions of the quadrupole moments of CO_2 with the metal centres (Bourrelly et al., 2005; Vimont et al., 2007). Adsorption has been studied with the following MOFs: MIL-53, MIL-47, MIL-53, Cu-BTC, MIL-53(Al), MIL-101(Cr), $Cu_3(BTC)_2$, ZIF-8, UMCM-1, MOF-177, Cu-MOF, Zn(dcpa) MOF and ZIF-8 (Cavenati et al., 2008; Ribeiro et al., 2019; Shen et al., 2023). In these works, Cu-MOF demonstrates high selectivity and has a high CO_2 adsorption capacity (Shen et al., 2023). In addition, the equilibria isotherm for Cu-MOF with CO_2 is almost linear (Abid et al., 2013; Bourrelly et al., 2005; Rallapalli et al., 2011; Shen et al., 2023; Xiang et al., 2011). On the other hand, MOF UIO-66(Zr) has also been used for the separation of the F-gases (R-32, R-125, and R-134) (Wanigarathna et al., 2018). Besides, the equilibria of R-32, R-134a and R-125 with Cu-BTC, ZIF-8, MIL-53 and MOF-177 have been studied. These materials are selective for R-125 and R-134a (Sosa et al., 2023). Finally, adsorption studies have also been carried out with MOF-5 for R-134a and R-143a (Wang et al., 2019). In this case, the adsorption of R-134a is preferred due to the fluorine atoms present in this gas (Wang et al., 2019). However, although MOFs are attractive due to their structural characteristics, very strict conditions are required for their preparation, and their precursors are expensive, which can limit their use on an industrial scale.

On the other hand, activated carbons (ACs) are cheap materials with large porosity, extended surface area, and pore size distribution (Gougazeh and Buhl, 2014; Islam and Saha, 2024a; Jeong et al., 2023; Maniarasu et al., 2023; Punpee et al., 2023; Sayari et al., 2011; Serafin and Dziejarski, 2024; Shen et al., 2023). Therefore, their use for GHG capture appears to be a viable alternative. ACs are good materials for the adsorptive storage of CH_4 (Liu et al., 2024). Moreover, their organic and mineral content favours the competitive adsorption of CO_2 over CH_4 (Busch and Gensterblum, 2011; Jeong et al., 2023). ACs can be designed with structural characteristics that selectively favour the separation of CO_2 over CH_4 (Shen et al., 2023). ACs such as Maxsorb I (ACP) and A-20 (ACF) have been used for R-32 adsorption (Askalany and Saha, 2015). Vruf AC (Calgon Carbon Corp) has also been tested in the adsorptive separation of the R-125/R-115 mixture and shown to be more selective for R-125 (Peng et al., 2010). Maxsorb, Chemviron, and Fluka ACs have been tested for the adsorption of R-134a (Akkimaradi et al., 2001), while Ecosorb, BAC, AC1, and AC2 have been tested for the adsorption of R-32, R-125 and R-134a (Sosa et al., 2020). The chemical activation compound influences the structural characteristics of activated carbon monoliths (Reljic et al., 2022). 12 monoliths were activated with different chemical compounds to generate larger porosity and favour the selective adsorption of CO_2 (Maniarasu et al., 2023). In addition, binders (carboxymethylcellulose) have been studied to favour the packing of ACM (Reljic et al., 2022). However, binders generate a decrease in the adsorption capacity for GHGs (Reljic et al., 2022; Sosa et al., 2020). The production of Bio-ACs from residual biomass has also been studied to reduce the production costs of adsorbents (Deng et al., 2016; Islam and Saha, 2024a, 2024b; Lozano-Castelló et al., 2002; Reljic et al., 2022; Vargas et al., 2012). Bio-ACs are materials that can have high microporosity, mesoporosity, surface area, and high adsorption capacity, and are easy to regenerate (Islam and Saha, 2024a; Maniarasu et al., 2023; Serafin and Dziejarski, 2024; Yahya et al., 2018). In addition, activated carbons prepared from palm waste have been studied due to their high porosity, which facilitates the adsorption of R-32 (Islam and Saha, 2024a). This work aims to close the gap from fundamental studies to industrial applications with biomaterials as an alternative to commercial ACs (Carney et al., 2024; Nie et al., 2025; Reljic et al., 2022; Vargas et al., 2012).

In the field of CH_4 separation and purification, there are standardised processes and plants at the industrial level. However, there is no standardised technology in the refrigeration sector for the separation and purification of F-gases. There are only some studies of separation processes, such as the separation of R-32 on R-125 by vacuum swing adsorption (VSA) with commercial activated carbons (Gonzalez-Olmos and Llovell, 2024; Ribeiro et al., 2023). In addition, semi-continuous separation processes have been optimized in the European project KET4F-Gas using commercial carbons, and the implementation of this process is being developed in the LIFE4F-gases project (KET4F-Gas, 2021; LIFE-4-Fgases, 2024). Considering the context and design of materials with structural characteristics that benefit the separation and purification of GHGs, there are sources of residual biomass that can be used to produce novel Bio-ACs to replace commercial ACs in these processes. One source of biomass is the residual coconut shells from Brazilian industries, for which it is important to find a valorisation route on an industrial scale.

The objective of this work is to compare the adsorption equilibria of GHGs (R-32, R-125, R-134a, R-143a, CO_2 and CH_4) on different porous solid matrices (two BIO-ACs, a commercial MOF, and a commercial AC) at three near-ambient temperatures (283.15 K, 303.15 K and 323.15 K). The two BIO-ACs were produced from residual coconut shells using two activation compounds: CO_2 to generate microporosity (CS-CO_2) and $ZnCl_2$ to generate both micro-/mesoporosity (CS-$ZnCl_2$). The commercial ACM and FE-BTC were selected to compare the performance of these innovative biomaterials (CS-CO_2 and CS-$ZnCl_2$) in GHGs separation. The experimental equilibria were fitted with the dual-site Langmuir model and the selectivities of the commercial mixtures R-410A (mixture of R-32 and R-125), R-407C (mixture of R-32, R-125, and R-134a), R404A (mixture of R-125, R-134a, and R-143a), and CO_2/CH_4 mixture were predicted using the ideal adsorption solution theory (IAST). The goal of this work is to advance the study of separating complex GHG mixtures for potential use in industrial separation processes.

2. Materials and methods

2.1. Materials

Difluoromethane, R-32 (purity ≥ 99.9 wt%) and pentafluoroethane, R-125 (purity ≥ 99.8 wt%), 1,1,1,2-tetrafluoroethane, R-134a (purity ≥ 99.8 wt%), and 1,1,1-trifluoroethane, R-143a (purity ≥ 99.9 wt%), were supplied by Polo Zero (Lisbon, Portugal). Carbon dioxide, CO_2 (purity ≥ 99.9 wt%) and methane, CH_4 (purity ≥ 99.9 wt%), were supplied by Air Liquid (Lisbon, Portugal) and helium (purity ≥ 99.9 wt%) was supplied by Praxair (Lisbon, Portugal). Activated carbon monolith, ACM, was developed and produced by Sutcliffe Speakman Carbons Ltd (Bristol, UK), and MOF-Fe-BTC was supplied by Basolite F300, Sigma-Aldrich, Portugal.

2.2. Synthesis of biomass-derived porous carbons

The biomaterials used in this work were prepared from residual coconut shell (CS) biomass from the Maceio industries, AL, Brazil. The biomaterials were treated by chemical activation with $ZnCl_2$, CS-$ZnCl_2$, and by physical activation with CO_2, CS-CO_2. In the chemical activation, the CS was impregnated with $ZnCl_2$ using an impregnation ratio of 2:5 (w/w) and was kept at 353.15 K for 4 h. Then, the impregnated sample was submitted to pyrolysis under constant nitrogen flow (5 L/h). The temperature was raised at 5 K/min up to 873.15 K and maintained for 3 h. Subsequently, the obtained biomaterial was pre-washed with an HCl solution (2 M) to remove the excess $ZnCl_2$. Then, the sample was washed with deionized water until neutral pH and dried at 378.15 K. In the physical activation using CO_2, the CS biomass was first carbonized at 1073.15 K under a constant nitrogen flow of 5 L/h and maintained for 4 h. After cooling down to room temperature, the obtained biomaterial was activated under a CO_2 flow (1 L/h) at 1073 K for 4 h, followed by cooling down to room temperature.

2.3. Characterization of biomass-derived porous carbons

2.3.1. Textural properties

The porous solid matrices were degassed overnight at 423.15 K to determine the materials' structural characteristics. The nitrogen adsorption-desorption isotherms at 77 K (ASAP 2010 Micromeritics) were determined for each of the porous solid matrices. The surface area was obtained using the Brunauer-Emmett-Teller equation (S_{BET}). Besides, the total pore volume (v_{total}) for each of the porous solid matrices was determined with the isotherms of N_2 at a relative pressure P/P^0 of 0.95. Then, the volume of the micropores (v_{micro}) was determined by the t-plot method. Finally, the determination of the volume of the mesopores (v_{meso}) was calculated by the difference of v_{total} with v_{micro}. Finally, the pore size distribution for the porous solid matrices was determined by the density functional theory (DFT) adsorption model.

2.3.2. Fourier-transform infrared spectroscopy (FTIR)

FTIR with KBr disk method (Perkin-Elmer Spectrum 1000 Spectrometer, Waltham, MA, USA) was used in the range of 400 – 4000 cm^{-1} (with a resolution of 1 cm^{-1}) to determine the functional groups present on the surface of the porous solid matrices.

2.3.3. Thermal gravimetric analysis (TGA)

The determination of decomposition temperature of the materials was determined using the TGA analysis. This analysis was performed between the temperature range of 303.15–1173 K with a heating rate of 5 K min^{-1} and under an argon atmosphere.

2.3.4. Elemental analysis (EA)

The Thermo Finnigan-CE Instruments Flash EA 1112 CHNS was used to quantify the relative amounts of carbon (C), hydrogen (H), nitrogen (N), and sulphur (S) in the porous solid matrices.

2.4. Adsorption equilibria in porous solid matrices for GHGs

The gravimetric method was employed to measure the adsorption and desorption of (R-32, R-125, R-134a, R-143a, CO_2 and CH_4) in the four porous solid matrices in the pressure range 0.01–1.5 MPa and at 283.15, 298.15 and 323.15 K. The gravimetric equipment (MSB, Rubotherm GmbH, Germany) is a high-pressure double-cell magnetic suspension balance (Sosa et al., 2024, 2022, 2020).

Samples of the porous solid matrices (approximately 0.35 g) were loaded into the cells of the adsorption unit and degassed at 373.15 K for 9 h. This degassing step was carried out to ensure that the structural characteristics of the porous solid matrices are available for the adsorption of the GHGs. The GHGs under study were added to the cells and expected to reach equilibrium. This process was repeated until the maximum pressure of the isotherm was reached. Finally, depressurisation was carried out. The quantification of the amount of GHGs adsorbed in porous solid matrices can be expressed in terms of the excess adsorbed amount, q_{ex}, and the absolute adsorbed amount, q. The adsorption amounts, q_{ex}, are defined as:

$$q_{ex} = \frac{w - m_s - m_h + V_h\rho_g}{m_s} + v_s\rho_g \quad (1)$$

where w is the apparent mass weighed on the balance, m_s is the degassed mass of the porous solid matrix in the measuring cell, m_h and V_h are the mass and volume of the measuring cell contributing to the buoyancy effects, and ρ_g is the gas density at experimental temperature and pressure, extracted from the NIST Chemistry Webbook, (National Institute of Standards and Technology (NIST), 2025). In addition, v_s is the specific volume of the adsorbent ($v_s = \frac{1}{\rho_s}$), where ρ_s is the density of the porous solid matrix, determined by helium pycnometry (Gumma and Talu, 2010; Nabais et al., 2018). In this work, the data were reported in terms of absolute adsorbed amount, q, as follows:

$$q = q_{ex} + V_P\rho_g \quad (2)$$

where, V_P is the specific pore volume of the adsorbent (determined by adsorption of N_2 at 77 K) and ρ_g is the density of the GHGs at experimental temperature and pressure, extracted from the NIST Chemistry Webbook (National Institute of Standards and Technology (NIST), 2025).

3. Results and discussion

3.1. Materials characterization

Table 1 shows the results of the nitrogen adsorption-desorption isotherms at 77 K for the four porous solid matrices, including their surface area (S_{BET}), total volume (v_{total}), micropore volume (v_{micro}), and mesopore volume (v_{meso}). The pore classification is defined by the IUPAC as micropores ≤ 20 Å, mesopores, between 20–500 Å, and macropores ≥ 500 Å (Sing, 1985; Thommes et al., 2015). CS-CO_2 has a S_{BET} of 602 m^2/g (see Table 1) and microporosity in the 5–15 Å range (Fig. 2). The N_2 adsorption-desorption isotherm for this material corresponds to a

Table 1
Textural parameters of the adsorbents studied in this work.

Adsorbent	S_{BET} (m^2/g)	v_{total} (cm^3g^{-1})[a]	v_{micro}(cm^3g^{-1})[b]	v_{meso}(cm^3g^{-1})[c]
CS-CO_2	602	0.245	0.211	0.034
CS-$ZnCl_2$	1391	0.859	0.240	0.619
ACM	1446	0.779	0.692	0.088
Fe-BTC	1213	0.625	0.487	0.139

[a] evaluated by the amount of N_2 adsorbed at $P/P^0 = 0.95$.
[b] determined by the t-plot method.
[c] determined by the difference between v_{total} and v_{micro}.

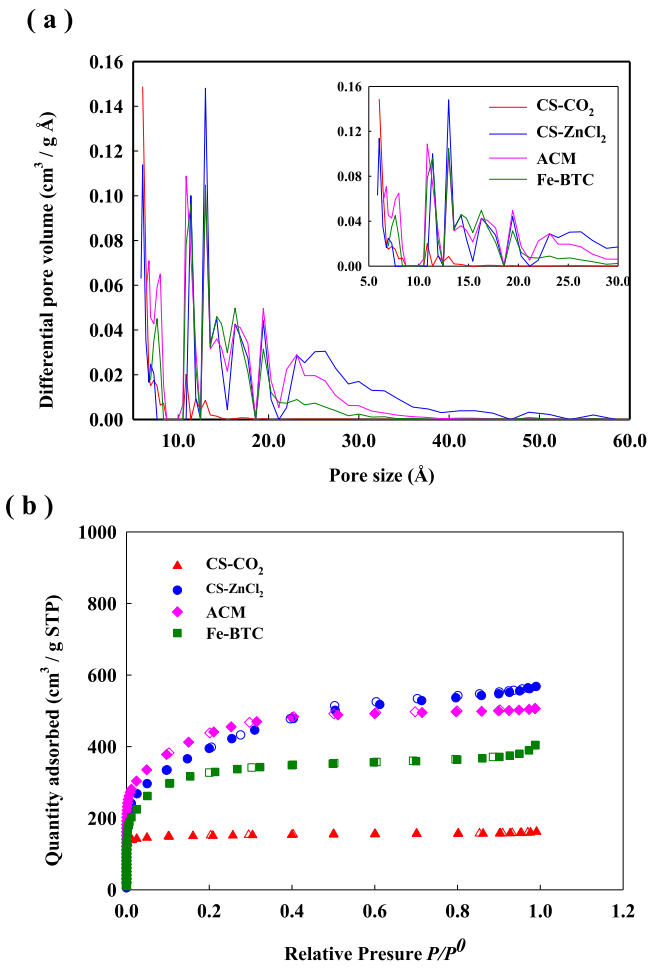

Fig. 2. Pore size distribution of the adsorbents studied in this work of: (a) CS-CO_2 (red line), CS-$ZnCl_2$ (blue line), ACM (pink line) and Fe-BTC(green line); (b) nitrogen adsorption (full symbols) and desorption (empty symbols) equilibrium isotherms at 77 K for CS-CO_2 (red up triangles), CS-$ZnCl_2$ (blue circles), ACM (pink diamond) and Fe-BTC(green square).

type I(a) with negligible hysteresis, characteristic of highly microporous materials with mainly narrow micropores, width $\leq$ 1 nm (Sing, 1985; Thommes et al., 2015).

CS-$ZnCl_2$ has a S_{BET} of 1391 m^2/g (see Table 1) and micro/mesoporosity in the 5–60 Å range (see Fig. 2). The N_2 adsorption-desorption isotherm of this material is the type I(b), which has pore size distributions over a broader range, including large micropores and narrow mesopores ($\leq$ 25 Å). Finally, ACM and Fe-BTC have micro/mesoporosity distributions in the 5–40 Å and 5–30 Å ranges, respectively, as shown in Fig. 2. Their surface areas are 1446 and 1213 m^2/g, respectively (see Table 1). The N_2 adsorption-desorption isotherms for these two materials are also type I(b) with negligible hysteresis. Fe-BTC is reported in the literature with a small surface area (480 m^2/g) and total pore volume of 0.27 cm^3/g (Nabais et al., 2018). These differences in structural characteristics can be attributed to the material preparation conditions (Sanchez-Sanchez et al., 2015). For example, in the literature, doped bimetallic materials have shown that the improvement in their structural properties is primarily due to the absence of charge-balancing anions (Rupam et al., 2022), resulting in structures with larger surface area and pore volume.

The FTIR spectra of CS-CO_2, CS-$ZnCl_2$, ACM, and Fe-BTC are shown in Fig. 3a. All materials have a common band around 3440 cm^{-1} attributed to stretching vibration of the hydroxyl groups of water, phenols and alcohols. Additionally, the bands located around 2923–2844 cm^{-1} correspond to the C—H stretching vibrations in the -CH_3 and -CH_2- functional groups. The bands around 1634–1619 cm^{-1} are assigned to the stretching vibrations of the *C═C* aromatic ring. The peak observed at 1382 cm^{-1} can also be attributed to the O—H bend frequency of phenol, while the ether structures present in the material cause stretching vibrations at 1130 cm^{-1}. In the FTIR spectrum of Fe-BTC, the bands at 1564–1372 cm^{-1} are due to the asymmetric and symmetric stretching vibrations of the carboxylate groups present in Fe-BTC (Delpiano et al., 2021). Additionally, the band at the 767 cm^{-1} is due to the bending of aromatic CH bonds.

The stability of these materials was determined by thermogravimetric analysis (TGA). Furthermore, TGA also allows the determination of the decomposition temperature and evaluates if the degassing process affects the structural characteristics of the adsorbents. Fig. 3b shows that the CS-CO_2 and CS-$ZnCl_2$ experience a 5 % mass loss at temperatures around 350 K, which may be due to adsorbed water or gases in their microporosity. Additionally, there is a 15 % mass loss for CS-$ZnCl_2$ at temperatures above 900 K due to the decomposition of the material. Biomaterials (CS-CO_2 and CS-$ZnCl_2$) are the most stable materials studied in this work (Parsa et al., 2023; Safa Gamal et al., 2019). On the other hand, ACM experiences a significant mass loss of 25 % at temperatures below 370 K, which is attributed to water or gases adsorbed in the material's porosity. Then, the mass loss remains constant up to a temperature of 600 K, from which this material presents a continuous decomposition until a temperature above 1200 K. This mass loss may be due to the decomposition of organic material or mineral matter present in the material. Fe-BTC experiences a 10 % mass loss at temperatures below 400 K, caused by the water from its framework. In the range of 500–700 K, a 40 % mass loss was observed due to the decomposition of its organic material (Delpiano et al., 2021; Karami et al., 2022). Finally, at temperatures above 700 K, the material undergoes its ultimate decomposition.

The results of the elemental analysis are given in Table 2. As expected, CS-CO_2 and CS-$ZnCl_2$ have a high carbon content, which can be related to their origin from residual biomass rich in cellulose and hemicellulose. The variation in elemental content between these biomaterials can be explained by differences in residence time during the preparation or the different activation compounds used. On the other hand, all porous solids also exhibit high carbon and hydrogen content, which may enhance the interactions with the GHGs, favouring the adsorption.

3.2. Adsorption equilibrium of GHGs

The adsorption equilibria of R-32, R-125, R-134a, R-143a, CO_2 and CH_4 on the four different porous solids (CS-CO_2, CS-$ZnCl_2$, ACM and Fe-BTC) are shown in Tables S1-S4, Fig. 4 and Fig. S1-S5. These equilibria were measured at 283.15, 303.15 and 323.15 K. The adsorption equilibria of R-32, R-125, R-134a, and R-143a were measured below 80 % of the saturation pressure of each gas to prevent capillary condensation in the adsorbents. The temperature dependence of the adsorption equilibria is evaluated because it is needed for an efficient design of any adsorption and separation process. No hysteresis was observed in all adsorption equilibria, indicating only physical adsorption.

The adsorption-desorption equilibria of the pure components were initially fitted using the Toth adsorption model (see Fig. S6), which did not provide a satisfactory fit. Therefore, the Dual Site Langmuir (DSL) model was selected because it accurately describes the adsorption process. The use of the DSL model is necessary due to the heterogeneity of the porous solid matrix surface, the variety of functional groups, and the development of porosity that produces multiple adsorption sites with varying affinities between the adsorbent and adsorbate (Jung et al., 2024; Lee and Ruthven, 1979; Ruthven et al., 1980). The dual-site Langmuir (DSL) model is described as follows:

$$q_t = q_{m1,i}\frac{b_{1i}p_i}{1+b_{1i}p_i} + q_{m2,i}\frac{b_{2i}p_i}{1+b_{2i}p_i} \quad (3)$$

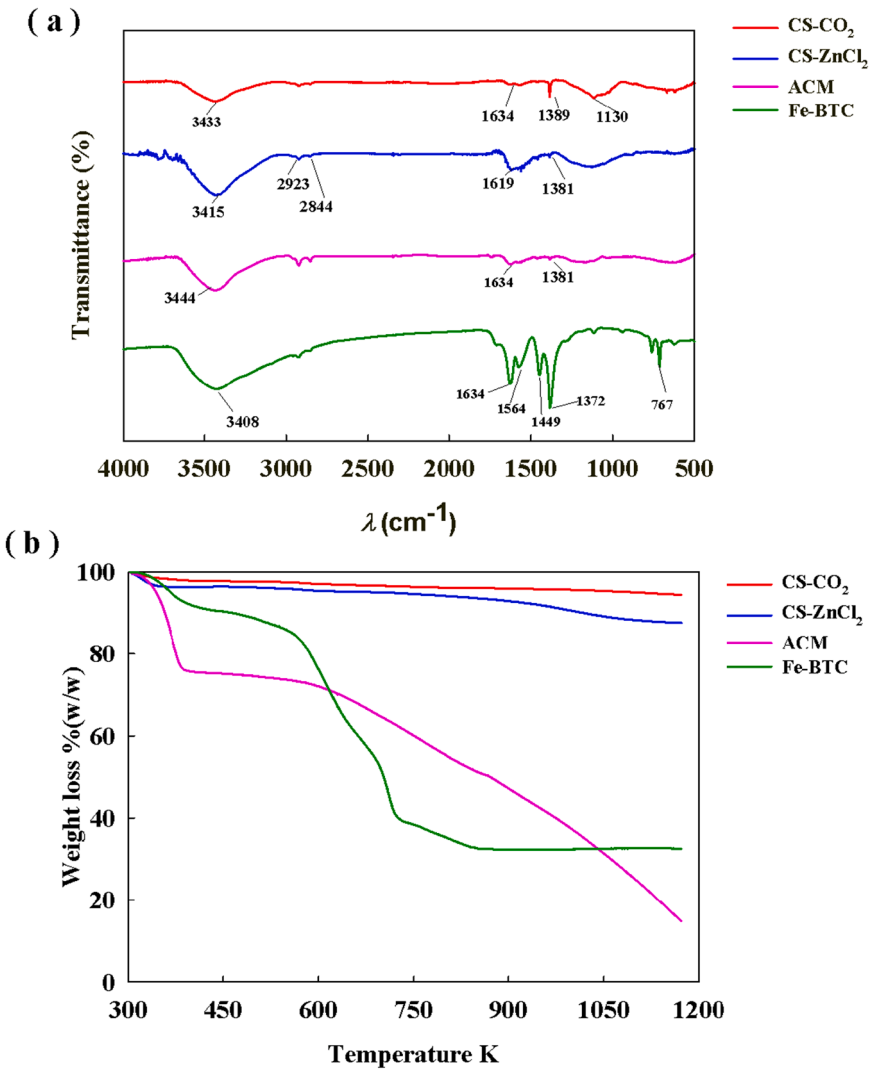

Fig. 3. Characterizations of (a) FTIR spectra and (b) thermogravimetric analysis (TGA) for the adsorbents studied in this work: CS-CO_2 (red line), CS-$ZnCl_2$ (blue line), ACM (pink line) and Fe-BTC (green line).

Table 2
Elemental analysis of the materials.

	CS-CO_2	CS-$ZnCl_2$	ACM	Fe-BTC
C (wt%)	73.5	80.6	54.6	32.8
H (wt%)	0.96	1.22	2.37	3.17
N (wt%)	0.12	0.85	0.23	0.2
S (wt%)	<L.D.	<L.D.	<L.D.	<L.D.

L.D. - limit of detection.

where $q_{m1,i}$ and $q_{m2,i}$ are the maximum adsorption capacity of component i in each of the two locations, b_{1i} and b_{2i} are the affinity constant (MPa^{-1}) of component i in the two locations, and p is the partial pressure (Ribeiro et al., 2023). The affinity parameters, b_{1i} and b_{2i}, can be expressed in the form of a temperature-dependent equation and can be obtained by Van't Hoff equation:

$$b_{ji} = b_{j\infty} \exp\left(\frac{-\Delta H_i}{R_g T}\right) \tag{4}$$

where b_∞ is the adsorption affinity constant at an infinite temperature, T is the temperature, R_g is the ideal gas constant and $-\Delta H_{ji}$ is the isosteric heat of adsorption of gas i on site j. On the other hand, Table S5 shows the parameters obtained from the DLS model, while the fittings are displayed in Fig. 4 and Fig. S1-S5. The average relative error (ARE) obtained from the experimental data was determined using the following equation:

$$ARE(\%) = \frac{100}{N_{exp}} \sum \frac{\left[q_{fit} - q_{exp}\right]}{q_{exp}} \tag{5}$$

where N_{exp} is the number of experimental points and q_{fit} and q_{exp} are the fit and experimental adsorbed quantity.

At pressures below 1.2 MPa, the order of adsorption capacity of R-32, R-125, R-134a and R-143a on the studied materials is ACM > CS-$ZnCl_2$ > Fe-BTC > CS-CO_2, directly related to the decrease of these materials' surface area (see Table 1). The surface area or the specific microporous volume controls the adsorption capacity of these materials. Then, materials with larger pore volumes and surface areas have greater GHG saturation capacities. ACM has the highest micropore volume and shows the extreme adsorption slope at low pressure. However, CS-$ZnCl_2$ surpasses it at mid-pressures due to the larger pore volumes associated with its mesoporosity. Then, the adsorption data are in agreement with the structural properties listed in Table 1.

The CO_2 adsorption capacity of the materials follows the order of: ACM > Fe-BTC > CS-$ZnCl_2$ > CS-CO_2 (see Fig. 4e). This behaviour agrees with the decrease of the total specific micropore volume.

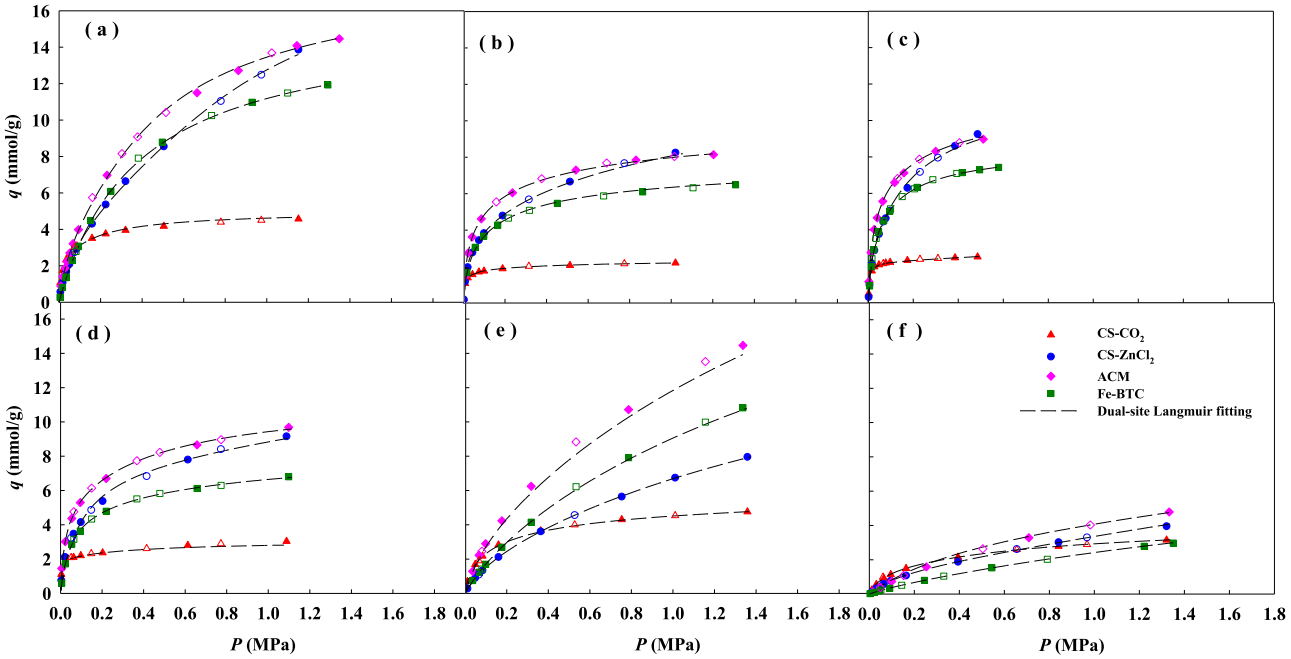

Fig. 4. Adsorption (full symbols) and desorption (empty symbols) equilibrium isotherms of: (a) R-32; (b) R-125; (c) R-134a; (d) R-143a; (e) CO_2; and (f) CH_4 at 303.15 K.

Although CS-CO_2 has a smaller saturation capacity than the other materials, this biomaterial has a CO_2 adsorption capacity similar to ACM and larger than the MOF at $P< 0.4$ MPa.

At pressures below 0.1 MPa, the order of methane adsorption is CS-CO_2 > CS-$ZnCl_2$ > ACM > Fe-BTC. This order is consistent with the increment of the surface area and total micropore volume of these activated carbons. Moreover, Fe-BTC is not favoured in the adsorption process due to the repulsive interactions of the iron present in this MOF structure. At pressures above 0.8 MPa, the order of the materials is ACM > CS-$ZnCl_2$ > CS-CO_2 > Fe-BTC and at pressures above 1.4 MPa presents the same order of the S_{BET}: ACM > CS-$ZnCl_2$ > Fe-BTC > CS-CO_2. If Fe-BTC is excluded once more, the order is favoured by the surface area and volume of micropores. In the case of Fe-BTC, this material generates repulsion between the iron III present in its structure and the methane, which can hinder the adsorption process (Sapnik et al., 2021).

3.3. Isosteric heat of adsorption

In the design of separation processes, it is important to consider the isosteric heat of adsorption (Q_{st}) because the separation can present temperature peaks that affect the capacity of the materials. Therefore, the theoretical Q_{st} was calculated from the experimental adsorption equilibria. Firstly, the experimental data were fitted to the virial equation, which is defined as follows:

$$P = \frac{q}{K_H} exp\left(2Aq + \frac{3}{2}Bq^2 + \frac{4}{3}Cq^3\right) \quad (6)$$

$$A = \sum_m^{\infty} \frac{A_m}{T^m} \quad (7)$$

$$B = \sum_m^{\infty} \frac{B_m}{T^m} \quad (8)$$

$$C = \sum_m^{\infty} \frac{C_m}{T^m} \quad (9)$$

where P is the partial pressure of the gas, q is the adsorbed capacity in equilibrium (absolute adsorption), K_H is Henry's constant, and A, B and C are the virial coefficients. These parameters are contingent upon temperature and are truncated after the second term (see Table S6).

Then, the value Q_{st} was determined using the Clausius-Clapeyron equation in an integrated manner (Ribeiro et al., 2020, 2016; Sosa et al., 2024):

$$(\log_e P)_{q} = constant - \frac{Q_{st}}{RT} \quad (10)$$

In this second step, linear isosteric plots were converted to $(\log_e P)_{q=const}$ *vs* $1/T$ for different adsorbed quantities (see Fig. S7-S10), enabling the determination of the Q_{st}. The Q_{st} for R-32, R-125, R-134a, and CO_2 is in the range of 20–60 kJ/mol (see Fig. 5), while for CH_4 it varies between 8–18 kJ/mol. The Q_{st} of GHGs on ACM, Fe-BTC, and CS-$ZnCl_2$ materials tends to have a line shape and a gentle slope. Initially, the adsorbate adheres to the narrow pores of the adsorbent, generating strong interactions and high isosteric heat. Once these high-energy sites are saturated, the adsorbate molecules begin to occupy lower-energy pores, reducing the isosteric heat (Jia et al., 2024; Palash et al., 2021; Ribeiro et al., 2016; Rupam et al., 2019). However, the Q_{st} of R-134a, CO_2 and CH_4 on CS-CO_2 increases and then begins to decrease. This is because gas molecules must occupy energetically stable locations, which allow them to interact and generate heat release (Jia et al., 2024; Palash et al., 2021; Rupam et al., 2019). The Q_{st} of R-32, R-125, and R-143a on CS-CO_2 exhibit unusual behaviour due to their structural characteristics. This material has a well-developed porosity (see Fig. 2a), with pores of different energy levels. These pores fill up and the available energy decreases, reducing the Q_{st}. However, once these sites are occupied, the adsorbed molecules interact with others, promoting adsorption and gradually increasing the heat release during the process (Babarao et al., 2007; Jia et al., 2024; Lyubchyk et al., 2011; Ribeiro et al., 2016).

3.4. Prediction of the GHG separation using the ideal adsorption solution theory (IAST)

The design and optimisation of efficient technology to separate and purify the commercial mixtures of GHGs, most used in European industries, has aroused great interest. In some cases, there is no stand-

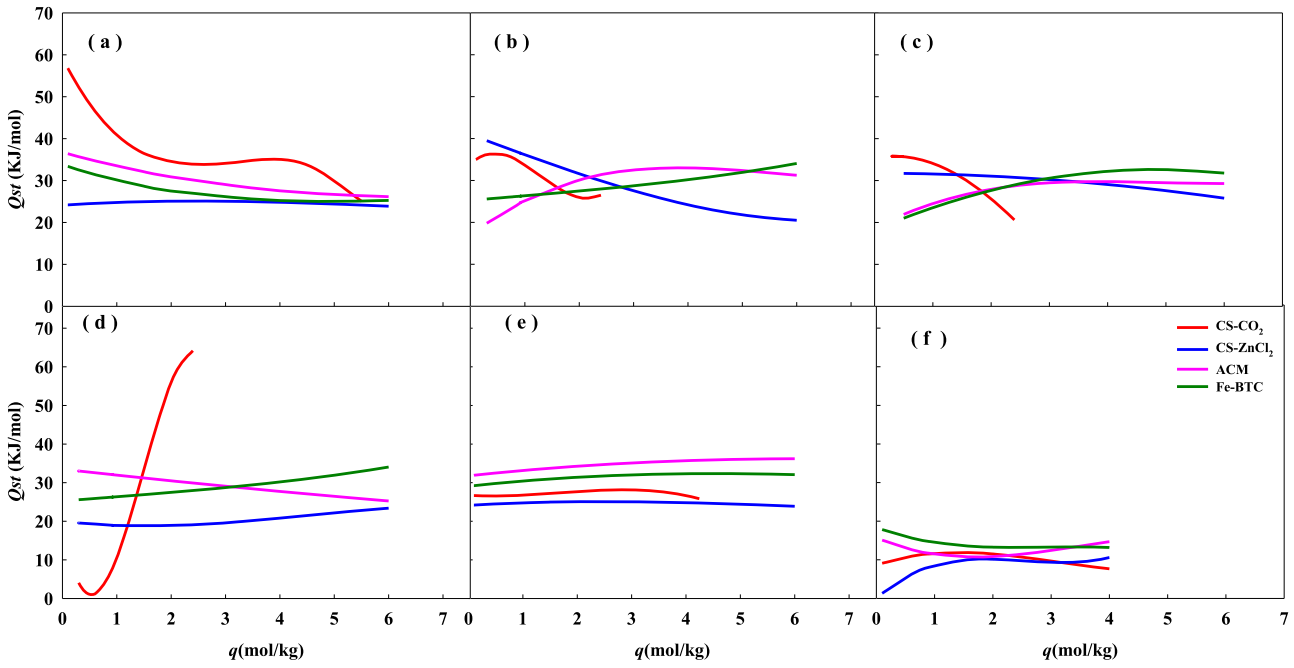

Fig. 5. Isosteric heat of adsorption of: (a) R-32; (b) R-125; (c) R-134a; (d) R-143a; (e) CO_2; and (f) CH_4 at 303.15 K.

ardised technology to capture and separate these GHGs at the end of the life cycle of the equipment containing them. The performance of the different separations for commercial blends can be theoretically calculated through selectivity. The prediction of the multicomponent composition of the adsorbed phase was determined using Ideal Adsorption Solution Theory (IAST) (Myers, 1968; Myers and Prausnitz, 1965; Myers and Valenzuela, 1986; Sosa et al., 2020), for the following commercial blends of GHGs: R-410A (R-32/R-125, 50/50 wt%, data in Fig. 6 and Table S7, R-407C (R-32/R-125/R-134a, 23/25/52 wt%, data in Fig. 7 and Table S8), R-404A (R-125/R-143a/R-134a, 44/52/4 wt%, data in Fig. 8 and Table S9) at 303.15 K in the pressure ranges of 0.1–1.0 MPa. A pressure limitation in these commercial blends was applied to avoid capillary condensation by saturation. The CO_2/CH_4 mixture (65/35 wt%) was determined at 303.15 K in the pressure range of 0.1–1 MPa (see Fig. 9 and Table S10). The selectivity for the solid-fluid system was determined as follows:

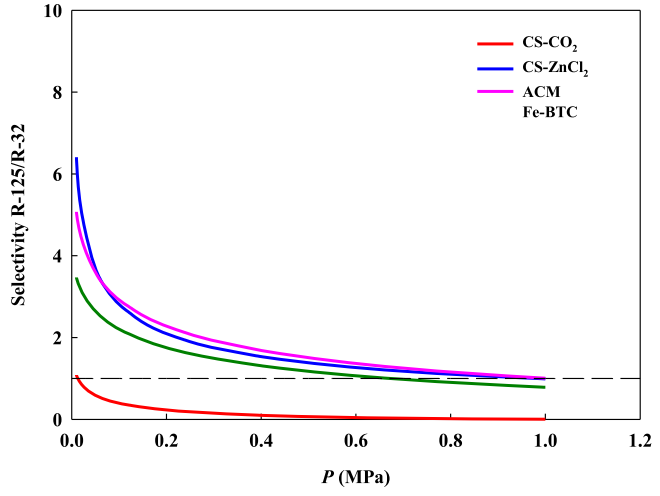

Fig. 6. Selectivity of CS-CO_2 (red line), CS-$ZnCl_2$ (blue line), ACM (pink line) and Fe-BTC (green line) to R-32 over R-125 as a function of pressure at 303.15 K, for R-410A blend ($y_{(R\text{-}32)} = 0.7$ and $y_{(R\text{-}125)} = 0.3$).

$$S_{ij} = \frac{x_i/x_j}{y_i/y_j} \tag{11}$$

where x_i and x_j are the adsorbed mole fractions of gas i and j, respectively, and $y_i$and $y_j$are the mole fractions of gas i of gas j in the gas phase at equilibrium, respectively.

The selectivity for the commercial blend R-410A is shown in Fig. 6 and Table S11 for the four porous solid matrices. At $P < 0.1$, the order of the materials is CS-$ZnCl_2$ > ACM > Fe-BTC > CS-CO_2, which coincides with the decrease in the total pore volume of the materials (see Table 1). In this case, the R-125 size is higher than the R-32, which plays an important role in separating this commercial refrigerant blend R-410A. Then, a larger number of molecules can be packed into the materials that have a larger volume. However, at P> 0.1 MPa, the best performance is obtained for commercial activated carbon ACM with values similar to CS-$ZnCl_2$. Under these pressures, materials with a higher surface area allow for the storage of a greater number of molecules. On the other hand, in the separation of R-32 over R-125, the CS-CO_2 material is more favoured because this material has the smallest pores, facilitating the adsorption of small gases.

The selectivity of the commercial blend R-407C is displayed in Fig. 7 and Table S12. To understand the selectivity of this refrigerant blend, it was divided into the binary mixtures R-125/R-32, R-134a/R-125 and R-134a/R-32. The binary mixtures R-125/R-32 and R-134a/R-32 tend to have similar behaviour. At $P < 0.1$ MPa, the order of the binary mixtures is given by CS-$ZnCl_2$ > ACM > Fe-BTC > CS-CO_2, which corresponds again to the decrease of the total pore volume of the materials (see Table 1). The molecules of R-125 and R-134a are larger than R-32 and it is easier to adsorb in materials with high total pore volume and larger pores, as expected. However, for P> 0.1 MPa, the selectivity tends to decrease in the following order: ACM > CS-$ZnCl_2$ > Fe-BTC > CS-CO_2. This order corresponds to the decreasing order of the surface area of the materials because a greater surface area can store more gas molecules. However, it is important to note that the activated carbons ACM and CS-$ZnCl_2$ have similar values over the range of pressures studied in this work.

Fig. 7b and Table S12 present the selectivity of the binary mixture R-134a/R-125. In this separation, the order of the materials is given by CS-

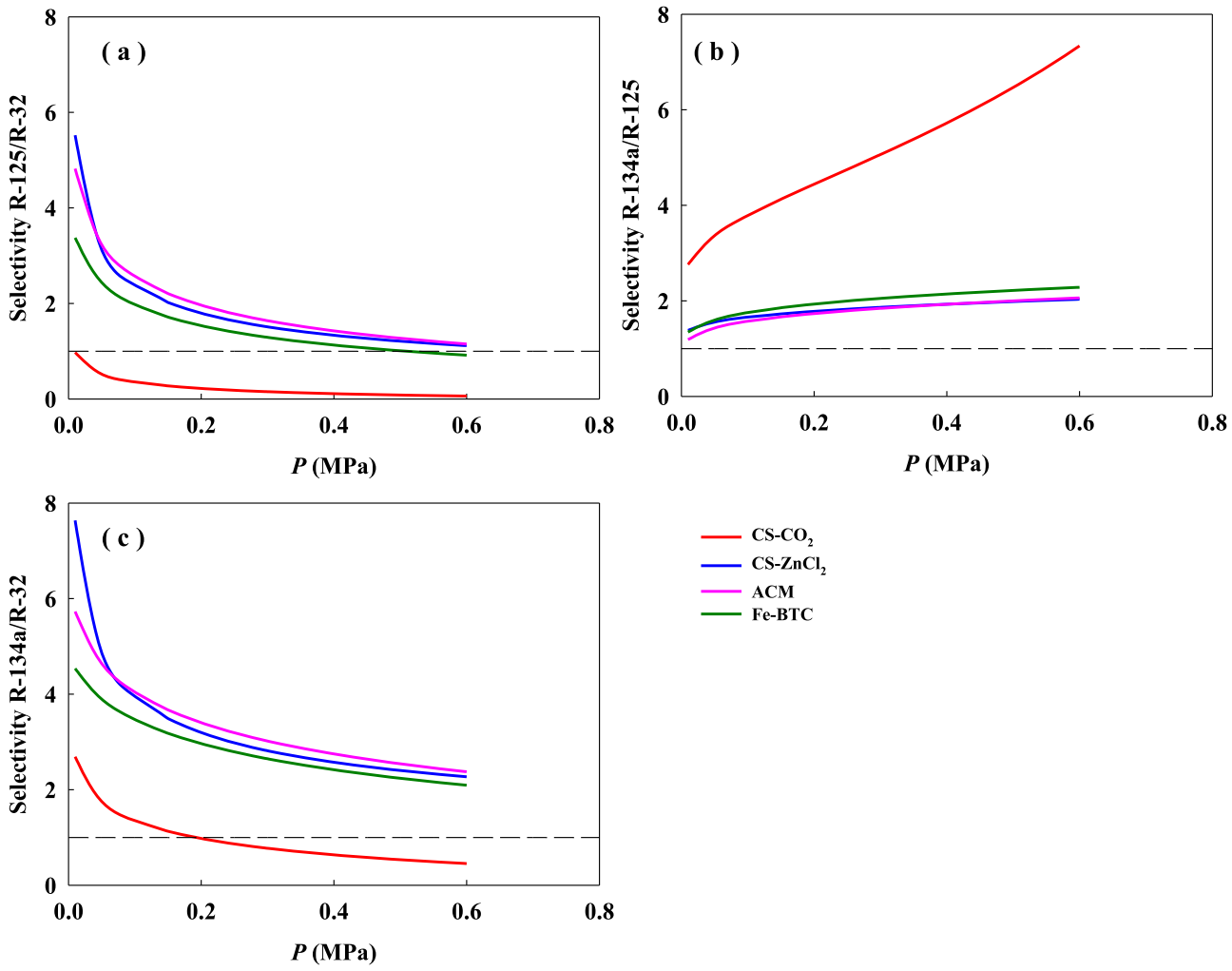

Fig. 7. Selectivity of CS-CO_2 (red line), CS-$ZnCl_2$ (blue line), ACM (pink line) and Fe-BTC (green line) to: (a) R-125 over R-32; (b) R-134a over R-125 and (c) R-134a over R-32, as a function of pressure at 303.15 K for the commercial R-407C blend (*y*R-32 = 0.38, *y*R-125 = 0.18, and *y*R-134a = 0.44).

CO_2 > Fe-BTC > ACM ≈ CS-$ZnCl_2$ and this order coincides with the increasing order of the total pore volume of the materials (see Table 1). In this case, the hydrogen atoms of F-gases can form hydrogen bonds with the oxygens present in the oxygenated functional groups at the CS-CO_2 surface (see Fig. 3a), favouring the separation in the mixture R-134a/R-125.

In Fig. 8 and Table S13, the separation of the ternary mixture R-404A is presented. The possible separation was analysed taking into account the binary mixtures R-134a/R-143a, R-134a/R-125 and R-143a/R-125. The order of materials in the separation of the binary mixture R-134a/R-143a at high pressures is: Fe-BTC > CS-$ZnCl_2$ > ACM > CS-CO_2. The order of selectivity for all materials, except Fe-BTC, follows the decrease in total pore volume (see Table 1). This total volume allows the separation and storage of gases. However, the structure and metallic centre of Fe-BTC generate a greater number of preferential adsorption sites for R-134a than for R-143a. The difference between these F-gases is in the number of fluorine atoms (R-134a has 4 fluorine atoms and R-143a has 3 atoms), which are highly electronegative. The negatively charged fluorine atoms of R-134a generate stronger interactions with the positively charged metallic centre of Fe-BTC, favouring the separation (Wanigarathna et al., 2020). Furthermore, Fig. 8 represents the selectivity of the binary mixture R-134a/R-125 and R-143a/R-125. The separation of these mixtures is influenced by the dipolar moment of the F-gases (R-143a > *R*-134a > *R*-125 with values of 2.32, 2.06, and 1.54 Debye, respectively) (Wanigarathna et al., 2020). The dipolar moment generates greater interactions with the functional groups on the surface of materials, improving pore filling and increasing competitive adsorption by the adsorbent (Madani et al., 2019; Wanigarathna et al., 2020). On the other hand, in the separation of the mixture R-134a over R-125, the order of materials is CS-CO_2 > Fe-BTC > ACM > CS-$ZnCl_2$, and this order respects the increment of the total volume of the pores of the materials (see Table 1).

The separation of CO_2 and CH_4 is illustrated in Fig. 9, and the selectivity values are presented in Table S14. In this case, the order of selectivity is as follows: ACM > Fe-BTC > CS-CO_2 > CS-$ZnCl_2$. The selectivity of the material favours the CO_2 separation over the CH_4 molecule. ACM exhibits a higher microporosity and surface area (see Fig. 2 and Table 1), which allows the packing of a greater number of molecules.

4. Conclusions

Biomaterials can be an efficient alternative to provide solutions for the capture and separation of GHGs. These novel alternatives have structural characteristics such as porosity and surface area that allow them to selectively adsorb GHGs gases. Besides, these biomaterials can be prepared using residual biomass to minimise production costs and to make them more attractive for their industrial application. In this work, two activated carbons were prepared from coconut shell biomass residues (CS-CO_2 and CS-$ZnCl_2$), using chemical activation with $ZnCl_2$ and

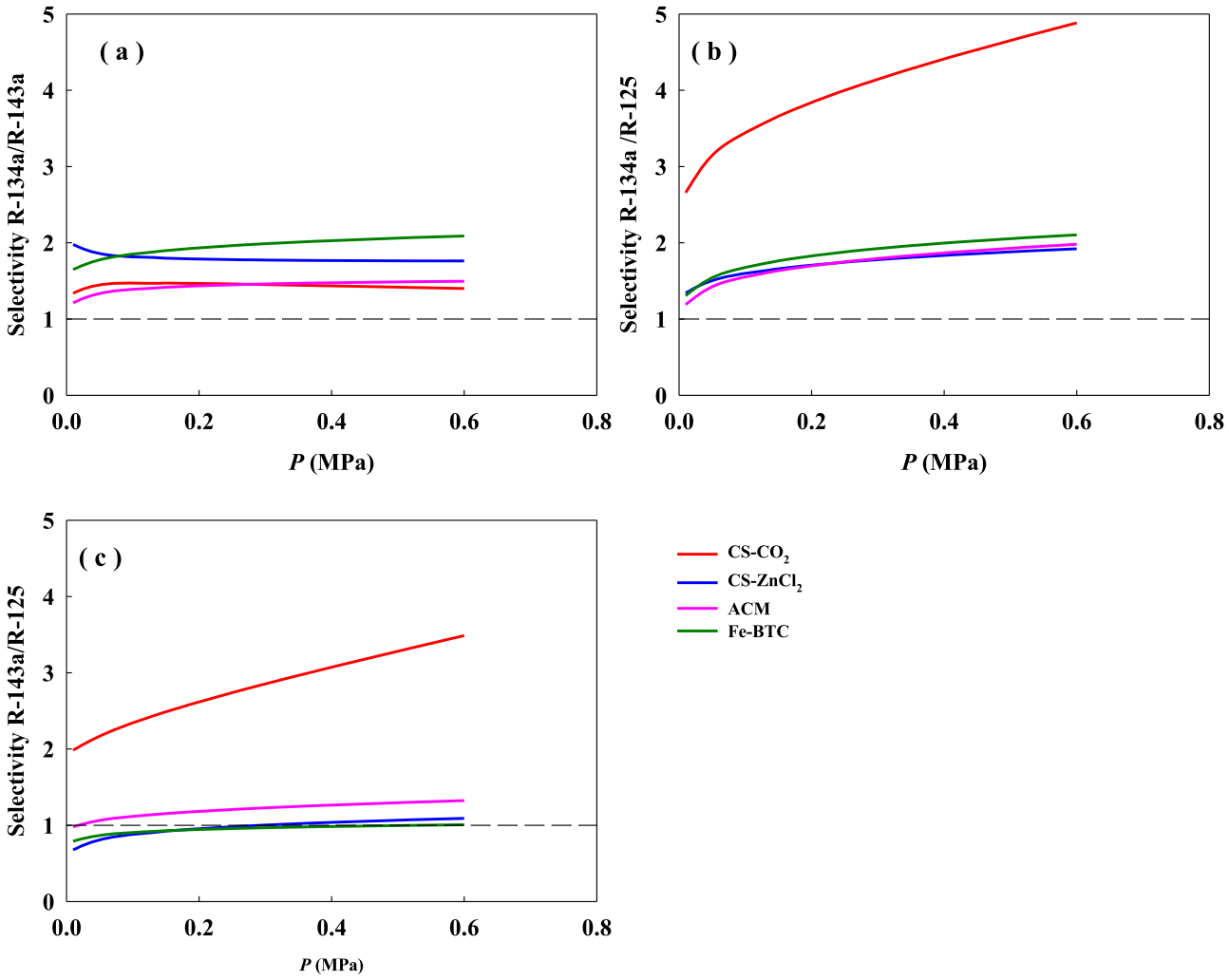

Fig. 8. Selectivity of CS-CO_2 (red line), CS-$ZnCl_2$ (blue line), ACM (pink line) and Fe-BTC (green line) to: (a) R-134a over R-143a, (b) R-134a over R-125 and (c) R-143a over R-125, as a function of pressure at 303.15 K for the commercial R-404A blend (yR-125 = 0.44, yR-143a = 0.56, and yR-134a = 0.04).

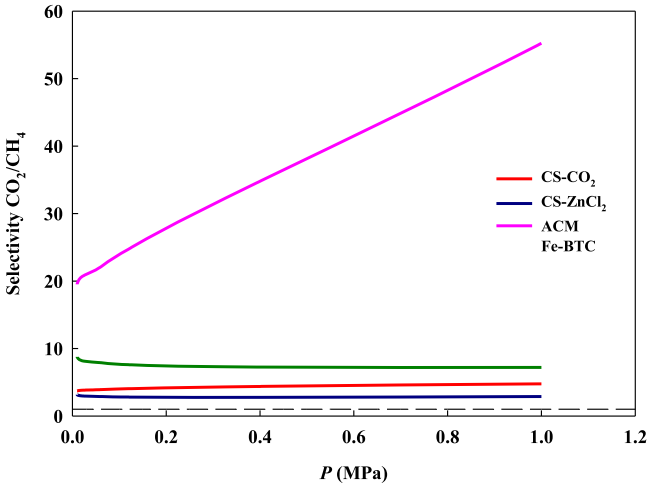

Fig. 9. Selectivity of CS-CO_2 (red line), CS-$ZnCl_2$ (blue line), ACM (pink line) and Fe-BTC (green line) to CO_2 over CH_4 as a function of pressure at 303.15 K, for the CO_2/CH_4 mixture (y_{CO_2} = 0.4 and y y_{CH_4} = 0.6).

physical activation with CO_2. The activation processes play a key role in developing stable and functional structures for adsorption applications. Both activation methods significantly contributed to the formation of a well-developed porous network, enhancing these biomaterials' stability.

In addition, two other solid porous materials, a commercial activated carbon ACM and a MOF Fe-BTC, were used to compare the performance of these biomaterials for the capture and separation of different GHGs studied in this work. All materials were characterised to understand how the textual properties can benefit the selective adsorption of GHGs. The nitrogen isotherms are characteristic of materials with large surface areas and are highly micro-mesoporous. In addition, adsorption equilibria of GHGs (R-32, R-125, R-134a, R-143a, CO_2 and CH_4) on two prepared biomaterials, CS-CO_2 and CS-$ZnCl_2$, and two commercial porous solid materials, ACM and Fe-BTC, were determined at 283.15, 303.15 and 323.15 K. The experimental adsorption equilibria were adjusted using the Dual Langmuir site adsorption model because this adsorption model allows us to describe the diversity of behaviours that are present in these systems. On the other hand, the IAST adsorption model was used to predict the separations of the mixtures R-410A, R-407C, R-404A and CO_2/CH_4. The results demonstrated that CS-$ZnCl_2$ is the most effective material for the separation of R-410A and R-407C blends at atmospheric pressure. This material has a large surface area, which allows it to store a notable number of GHGs molecules. Besides, CS-$ZnCl_2$ has large mesopores that allow these molecules to enter in the smallest micropores. On the other hand, CS-CO_2 obtained the highest

selectivity for the separation of the R-404A blend. This behaviour may be related to the oxygens present on the material surface that interact with the hydrogens present in the F-gas molecules.

Then, biomaterials prepared in this work (CS-CO_2, CS-$ZnCl_2$) offer higher selectivity compared to ACM and Fe-BTC, making them ideal for industrial applications where the separation of F-gases is crucial. Although their adsorption capacity is lower, their superior selectivity enables more efficient separation processes. Then, these biomaterials are the better choice for industrial applications that require high purity and efficiency. Finally, the activated carbon ACM is the material with the highest selectivity in the separation of the CO_2/CH_4 mixture. In this case, the GHGs molecules are preferentially adsorbed in micropores and large surface areas, which benefits the packing of these molecules. Finally, this work provides vital information to design novel capture and separation processes of GHGs using novel activated carbons prepared with waste biomass. Then, the results of this work are essential for developing efficient alternative materials for the implementation of the separation of commercial refrigerants and other GHGs mixtures on a pilot scale.

Funding

The authors acknowledge the financial support from the European Union's Horizon Europe research and innovation programme under grant agreement No 101082048 – the MAR2PROTECT project. This work was also financed by national funds from FCT/MCTES (Portugal) through Associate Laboratory for Green Chemistry–LAQV (UIDB/50006/2020 | UIDP/50006/2020), grant 2022.11909.BD (J.E.S), the contracts of Individual Call to Scientific Employment Stimulus 2020.00835.CEECIND (J.M.M.A.) / 2021.01432.CEECIND (A.B.P.) / CEECIND/004431/2022 (I.M.), and the Norma Transitória DL 57/2016 Program Contract (R.P.P.L.R. and M.B.).

Data availability

The research data underlying this manuscript has been published in the MAR2PROTECT Zenodo Repository: https://doi.org/10.5281/zenodo.13927477.

Appendix A. Supplementary Information

Supplementary data associated with this article can be found in the online version at.

CRediT authorship contribution statement

Julio E. Sosa: Writing – original draft, Visualization, Investigation, Formal analysis, Data curation. **Rui.P.P.L. Ribeiro:** Writing – review & editing, Supervision, Methodology, Formal analysis. **Inês Matos:** Writing – review & editing, Investigation, Formal analysis. **Maria Bernardo:** Writing – review & editing, Investigation, Formal analysis. **Isabel M. Fonseca:** Writing – review & editing, Methodology, Investigation. **José P.B. Mota:** Writing – review & editing, Methodology, Investigation. **João M.M. Araújo:** Writing – review & editing, Supervision, Resources, Project administration, Methodology, Funding acquisition, Conceptualization. **Ana B. Pereiro:** Writing – review & editing, Supervision, Resources, Project administration, Methodology, Funding acquisition.

Declaration of interests

The authors declare the following financial interests/personal relationships which may be considered as potential competing interests:

Ana B. Pereiro reports financial support was provided by Horizon Europe. If there are other authors, they declare that they have no known competing financial interests or personal relationships that could have appeared to influence the work reported in this paper.

References

Abd, A.A., Othman, M.R., Helwani, Z., Kim, J., 2023. Waste to wheels: performance comparison between pressure swing adsorption and amine-absorption technologies for upgrading biogas containing hydrogen sulfide to fuel grade standards. Energy 272, 127060. https://doi.org/10.1016/j.energy.2023.127060.

Abdelaziz O, P.F.P.R.K.L., 2023. Refrigeration, Air Conditioning and Heat Pumps Technical Options Committee (RTOC) 2022 assessment report (Montreal Protocol on Substances That Deplete the Ozone Layer). URL https://ozone.unep.org/system/files/documents/RTOC-assessment%20-report-2022.pdf (accessed 12.17.24).

Abid, H.R., Shang, J., Ang, H.-M., Wang, S., 2013. Amino-functionalized Zr-MOF nanoparticles for adsorption of CO_2 and CH_4. Int. J. Smart. Nano Mater. 4, 72–82. https://doi.org/10.1080/19475411.2012.688773.

Akkimaradi, B.S., Prasad, M., Dutta, P., Srinivasan, K., 2001. Adsorption of 1,1,1,2-tetrafluoroethane on activated charcoal. J. Chem. Eng. Data 46, 417–422. https://doi.org/10.1021/je000277e.

Andreoni A., 2024. Climate change drove drought in the amazon. URL https://www.nytimes.com/2024/01/24/climate/amazon-drought-low-water.html (accessed 2.18.25).

Askalany, A.A., Saha, B.B., 2015. Experimental and theoretical study of adsorption kinetics of difluoromethane onto activated carbons. Int. J. Refrig. 49, 160–168. https://doi.org/10.1016/j.ijrefrig.2014.10.009.

Babarao, R., Hu, Z., Jiang, J., Chempath, S., Sandler, S.I., 2007. Storage and separation of CO2 and CH4 in silicalite, C168 schwarzite, and IRMOF-1: a comparative study from Monte Carlo simulation. Langmuir. 23, 659–666. https://doi.org/10.1021/la062289p.

Ball, J.C., Wellington, T.J., 1993. Formation of trifluoroacetic acid from the atmospheric degradation of hydrofluorocarbon 134a: a Human health concern? Air. Waste 43, 1260–1262. https://doi.org/10.1080/1073161X.1993.10467204.

Beans, E.W., 2023. A heat transfer model for global warming. Case Stud. Therm. Eng. 43, 102677. https://doi.org/10.1016/j.csite.2022.102677.

Bolan, S., Padhye, L.P., Jasemizad, T., Govarthanan, M., Karmegam, N., Wijesekara, H., Amarasiri, D., Hou, D., Zhou, P., Biswal, B.K., Balasubramanian, R., Wang, H., Siddique, K.H.M., Rinklebe, J., Kirkham, M.B., Bolan, N., 2024. Impacts of climate change on the fate of contaminants through extreme weather events. Sci. Total Environ. 909, 168388. https://doi.org/10.1016/j.scitotenv.2023.168388.

Bourrelly, S., Llewellyn, P.L., Serre, C., Millange, F., Loiseau, T., Férey, G., 2005. Different adsorption behaviors of methane and carbon dioxide in the isotypic nanoporous metal terephthalates MIL-53 and MIL-47. J. Am. Chem. Soc. 127, 13519–13521. https://doi.org/10.1021/ja054668v.

Busch, A., Gensterblum, Y., 2011. CBM and CO2-ECBM related sorption processes in coal: a review. Int. J. Coal. Geol. 87, 49–71. https://doi.org/10.1016/j.coal.2011.04.011.

Cardoso, B.J., Lamas, F.B., Gaspar, A.R., Ribeiro, J.B., 2017. Frigorigènes utilisés dans l'industrie alimentaire portugaise: statut actuel. Int. J. Refrig. 83, 60–74. https://doi.org/10.1016/j.ijrefrig.2017.07.013.

Carney, J.B., Mahurin, S.M., Zhang, Y., Wang, Y., Poirier, G., Zhao, Y., Chen, G., Austin, D., Michaelis, E., Yue, Y., 2024. Highly porous biocarbon monoliths for methane storage. Microporous Mesoporous Mater. 370, 112921. https://doi.org/10.1016/j.micromeso.2023.112921.

Cavenati, S., Grande, C.A., Rodrigues, A.E., Kiener, C., Müller, U., 2008. Metal organic framework adsorbent for biogas upgrading. Ind. Eng. Chem. Res. 47, 6333–6335. https://doi.org/10.1021/ie8005269.

da Costa, M., Kalmar, A.F., Struys, M.M.R.F., 2021. Inhaled anesthetics: environmental role, occupational risk, and clinical use. J. Clin. Med. 10. https://doi.org/10.3390/jcm10061306.

Delpiano, G.R., Tocco, D., Medda, L., Magner, E., Salis, A., 2021. Adsorption of Malachite green and Alizarin red S dyes using Fe-BTC Metal Organic framework as adsorbent. Int. J. Mol. Sci. 22. https://doi.org/10.3390/ijms22020788.

Deng, J., Xiong, T., Wang, H., Zheng, A., Wang, Y., 2016. Effects of cellulose, hemicellulose, and lignin on the structure and morphology of porous carbons. ACS. Sustain. Chem. Eng. 4, 3750–3756. https://doi.org/10.1021/acssuschemeng.6b00388.

Díaz Tautiva, J.A., Huaman, J., Ponce Oliva, R.D., 2024. Trends in research on climate change and organizations: a bibliometric analysis (1999–2021). Manag. Rev. Q. 74, 227–261. https://doi.org/10.1007/s11301-022-00298-1.

Durkee, J., 2006. 2 - US and global environmental regulations. In: Durkee, J. (Ed.), Management of Industrial Cleaning Technology and Processes. Elsevier Science, Oxford, pp. 43–98. https://doi.org/10.1016/B978-008044888-6/50016-8.

European Commission, 2019. The European Green Deal. Eur. Comm. 53, 24. https://doi.org/10.1017/CBO9781107415324.004.

Ferreira, I.C., Ferreira, T.J., Barbosa, A.D.S., de Castro, B., Ribeiro, R.P.P.L., Mota, J.P.B., Alves, V.D., Cunha-Silva, L., Esteves, I.A.A.C., Neves, L.A., 2021. Cr-based MOF/IL composites as fillers in mixed matrix membranes for CO2 separation. Sep. Purif. Technol. 276, 119303. https://doi.org/10.1016/j.seppur.2021.119303.

Flores, B.M., Montoya, E., Sakschewski, B., Nascimento, N., Staal, A., Betts, R.A., Levis, C., Lapola, D.M., Esquível-Muelbert, A., Jakovac, C., Nobre, C.A., Oliveira, R.S., Borma, L.S., Nian, D., Boers, N., Hecht, S.B., ter Steege, H., Arieira, J., Lucas, I.L., Berenguer, E., Marengo, J.A., Gatti, L.V., Mattos, C.R.C., Hirota, M., 2024. Critical transitions in the Amazon forest system. Nature 626, 555–564. https://doi.org/10.1038/s41586-023-06970-0.

Gonzalez-Olmos, R., Llovell, F., 2024. Life cycle assessment of fluorinated gas recovery from waste refrigerants through vacuum swing adsorption. Sustain. Mater. Technol. 39, e00811. https://doi.org/10.1016/j.susmat.2023.e00811.

Gougazeh, M., Buhl, J.-C., 2014. Synthesis and characterization of zeolite A by hydrothermal transformation of natural Jordanian kaolin. J. Assoc. Arab Univ. Basic Appl. Sci. 15, 35–42. https://doi.org/10.1016/j.jaubas.2013.03.007.
Gumma, S., Talu, O., 2010. Net adsorption: a thermodynamic framework for supercritical gas adsorption and storage in porous solids. Langmuir. 26, 17013–17023. https://doi.org/10.1021/la102186q.
Henne, S., Shallcross, D.E., Reimann, S., Xiao, P., Brunner, D., O'Doherty, S., Buchmann, B., O'Doherty, S., Buchmann, B., 2012. Future emissions and atmospheric fate of HFC-1234yf from mobile air conditioners in europe. Env. Sci. Technol. 46, 1650–1658. https://doi.org/10.1021/es2034608.
Holland, R., Khan, M.A.H., Driscoll, I., Chhantyal-Pun, R., Derwent, R.G., Taatjes, C.A., Orr-Ewing, A.J., Percival, C.J., Shallcross, D.E., 2021. Investigation of the production of trifluoroacetic acid from two halocarbons, HFC-134a and HFO-1234yf and its fates using a global three-dimensional chemical transport model. ACS. Earth. Space Chem. 5, 849–857. https://doi.org/10.1021/acsearthspacechem.0c00355.
Hossain, M.I., Rabideau, B.D., Glover, T.G., 2024. The impact of trace amounts of CO2 on the high-pressure adsorption of CH4 on 5A zeolite. Microporous Mesoporous Mater. 369, 112948. https://doi.org/10.1016/j.micromeso.2023.112948.
Islam, M.A., Saha, B.B., 2024a. Harnessing waste palm-based activated carbon/difluoromethane pair for sustainable low-emission cooling systems. J. Env. Chem. Eng. 12, 114869. https://doi.org/10.1016/j.jece.2024.114869.
Islam, M.A., Saha, B.B., 2024b. Optimal utilization of waste biomass for the development of minimal emission sustainable cooling systems. Advancements in Non-Conventional Cooling and Thermal Storage Strategies. John Wiley & Sons, Ltd, pp. 39–63. https://doi.org/10.1002/9781394189953.ch3.
Isler-Kaya, A., Karaosmanoglu, F., 2023. Life cycle assessment of a climate-friendly data center cooling device. Energy Build. 288, 113006. https://doi.org/10.1016/j.enbuild.2023.113006.
Jeong, S.R., Park, J.H., Lee, J.H., Jeon, P.R., Lee, C.-H., 2023. Review of the adsorption equilibria of CO2, CH4, and their mixture on coals and shales at high pressures for enhanced CH4 recovery and CO2 sequestration. Fluid Ph. Equilib. 564, 113591. https://doi.org/10.1016/j.fluid.2022.113591.
Jia, J., Xing, Y., Li, B., Wu, Y., Wang, D., 2024. Molecular simulation study of adsorption-diffusion of CH4, CO2 and H2O in gas-fat coal. Sci. Rep. 14, 24131. https://doi.org/10.1038/s41598-024-74647-3.
Jordan, A., Frank, H., 1999. Trifluoroacetate in the environment. Evidence for sources other than HFC/HCFCs. Env. Sci. Technol. 33, 522–527. https://doi.org/10.1021/es980674y.
Jung, J., Do, H., Chung, K., Cho, M., Lee, C.-H., 2024. Adsorption equilibria and kinetics of CO2, CH4, CO, N2, O2, and H2 on silica-based adsorbents for H2 enhancement processes from steel off-gas for the direct reduced iron process. Chem. Eng. J. 479, 147678. https://doi.org/10.1016/j.cej.2023.147678.
Karami, A., Ahmed, A., Sabouni, R., Husseini, G.A., Sharabati, M.A., AlSawaftah, N., Paul, V., 2022. Hybrid liposome/metal–organic framework as a promising dual-responsive nanocarriers for anticancer drug delivery. Colloids. Surf. B Biointerfaces. 217, 112599. https://doi.org/10.1016/j.colsurfb.2022.112599.
KET4F-Gas, 2021. Reducción del impacto ambiental de los gases fluorados en el espacio Sudoe mediante tecnologías facilitadoras clave. 2023. URL http://www.ket4f-gas.eu/?page_id=350 (accessed 1.14.25).
Lee, L.-K., Ruthven, D.M., 1979. Analysis of thermal effects in adsorption rate measurements. J. Chem. Soc. Faraday Trans. 1 75, 2406–2422. https://doi.org/10.1039/F19797502406.
LIFE-4-Fgases, 2024. LIFE-4-Fgases. URL. https://www.life4fgases.eu/ (accessed 1.14.25).
Liu, J., Wang, Z., Peng, X., Ji, H., 2024. Analysis of the influence of different pore ratios on methane adsorption characteristics of coal. Fuel 358, 130273. https://doi.org/10.1016/j.fuel.2023.130273.
Lozano-Castelló, D., Cazorla-Amorós, D., Linares-Solano, A., Quinn, D.F., 2002. Activated carbon monoliths for methane storage: influence of binder. Carbon. N. Y. 40, 2817–2825. https://doi.org/10.1016/S0008-6223(02)00194-X.
Lyubchyk, A., Esteves, I.A.A.C., Cruz, F.J.A.L., Mota, J.P.B., 2011. Experimental and theoretical studies of supercritical methane adsorption in the MIL-53(Al) metal organic framework. J. Phys. Chem. C 115, 20628–20638. https://doi.org/10.1021/jp207326d.
Madani, S.H., Biggs, M.J., Rodríguez-Reinoso, F., Pendleton, P., 2019. Decoding gas-solid interaction effects on adsorption isotherm shape: II. Polar adsorptives. Microporous Mesoporous Mater. 278, 232–240. https://doi.org/10.1016/j.micromeso.2018.11.039.
Maniarasu, R., Rathore, S.K., Murugan, S., 2023. Biomass-based activated carbon for CO2 adsorption–a review. Energy Environ. 34, 1674–1721. https://doi.org/10.1177/0958305X221093465.
Miranda, N.D., Giovani Palafox-Alcantar, P., Khosla, R., McCulloch, M.D., 2023. Metrics for the emissions of F-gas refrigerants. Sustain. Energy Technol. Assess. 58, 103348. https://doi.org/10.1016/j.seta.2023.103348.
Mota-Babiloni, A., Makhnatch, P., Khodabandeh, R., 2017. Études récentes sur la substitution des HFC par des frigorigènes synthétiques alternatifs à faible GWP : performances énergétiques et impacts environnementaux. Int. J. Refrig. 82, 288–301. https://doi.org/10.1016/j.ijrefrig.2017.06.026.
Myers, A.L., 1968. Adsorption of gas mixtures-a thermodynamic approach. Ind. Eng. Chem. 60, 45–49. https://doi.org/10.1021/ie50701a007.
Myers, A.L., Prausnitz, J.M., 1965. Thermodynamics of mixed-gas adsorption. AIChe J. 11, 121.
Myers, A.L., Valenzuela, D., 1986. Computer algorithm and graphical method for calculating adsorption equilibria of gas mixtures. J. Chem. Eng. Jpn. 19, 392–396. https://doi.org/10.1252/JCEJ.19.392.
Nabais, A.R., Ribeiro, R.P.P.L., Mota, J.P.B., Alves, V.D., Esteves, I.A.A.C., Neves, L.A., 2018. CO2/N2 gas separation using Fe(BTC)-based mixed matrix membranes: a view on the adsorptive and filler properties of metal-organic frameworks. Sep. Purif. Technol. 202, 174–184. https://doi.org/10.1016/j.seppur.2018.03.028.
Nath, K., Wright, K.R., Ahmed, A., Siegel, D.J., Matzger, A.J., 2024. Adsorption of natural gas in metal–Organic frameworks: selectivity, cyclability, and comparison to methane adsorption. J. Am. Chem. Soc. 146, 10517–10523. https://doi.org/10.1021/jacs.3c14535.
National Institute of Standards and Technology (NIST), 2025. NIST. URL. https://www.nist.gov/ (accessed on 21 June 2024). (accessed 6.25.24).
Nie, L., Li, S., Cao, M., Han, N., Chen, Y., 2025. A brief review of preparation and applications of monolithic aerogels in atmospheric environmental purification. J. Environ. Sci. 149, 209–220. https://doi.org/10.1016/j.jes.2024.01.040.
Obi, C.C., Nwabanne, J.T., Igbokwe, P.K., Idumah, C.I., Okpechi, V.U., Oyeoka, H.C., 2024. Novel advances in synthesis and catalytic applications of metal-organic frameworks - based nanocatalysts for CO2 capture and transformation. J. Env. Chem. Eng. 12, 112835. https://doi.org/10.1016/j.jece.2024.112835.
Palash, M.L., Rupam, T.H., Pal, A., Chakraborty, A., Saha, B.B., Wang, R., 2021. Design principles for synthesizing high grade activated carbons for adsorption heat pumps. Chem. Eng. J. Adv. 6, 100086. https://doi.org/10.1016/j.ceja.2021.100086.
Parsa, M., Qi, Y., Di Nuzzo, J.J., Moussakhani, Y., Tirto, A., Chaffee, A.L., 2023. Regenerable carbon honeycomb monoliths directly prepared from brown coal: a novel carbon product. Chem. Eng. J. 471, 144699. https://doi.org/10.1016/j.cej.2023.144699.
Peng, Y., Zhang, F., Zheng, X., Wang, H., Xu, C., Xiao, Q., Zhong, Y., Zhu, W., 2010. Comparison study on the adsorption of CFC-115 and HFC-125 on activated carbon and silicalite-1. Ind. Eng. Chem. Res. 49, 10009–10015. https://doi.org/10.1021/ie1010806.
Pizzorni, M., Innocenti, A., Tollin, N., 2024. Droughts and floods in a changing climate and implications for multi-hazard urban planning: a review. City Environ. Interact. 24, 100169. https://doi.org/10.1016/j.cacint.2024.100169.
Publications Office of the European Union, 2023. GHG emissions of all world countries [WWW Document]. https://doi.org/10.2760/953322.
Punpee, S., Tongpadungrod, P., Suttikul, T., Phalakornkule, C., 2023. Characteristics of CO2 adsorption and desorption on activated carbon in comparison with zeolite 13X and carbon molecular sieve and applications in biogas upgrading using vacuum pressure swing adsorption. J. Chem. Technol. Biotechnol. 98, 2677–2690. https://doi.org/10.1002/jctb.7320.
Rallapalli, P., Prasanth, K.P., Patil, D., Somani, R.S., Jasra, R.V., Bajaj, H.C., 2011. Sorption studies of CO2, CH4, N2, CO, O2 and Ar on nanoporous aluminum terephthalate [MIL-53(Al)]. J. Porous Mater. 18, 205–210. https://doi.org/10.1007/s10934-010-9371-7.
Reljic, S., Cuadrado-Collados, C., Farrando-Perez, J., Jardim, E.O., Martinez-Escandell, M., Silvestre-Albero, J., 2022. Carbon-based monoliths with improved thermal and mechanical properties for methane storage. Fuel 324, 124753. https://doi.org/10.1016/j.fuel.2022.124753.
Ribeiro, R.P.P.L., Antunes, C.L., Garate, A.U., Portela, A.F., Plaza, M.G., Mota, J.P.B., Esteves, I.A.A.C., 2019. Binderless shaped metal-organic framework particles: impact on carbon dioxide adsorption. Microporous Mesoporous Mater. 275, 111–121. https://doi.org/10.1016/j.micromeso.2018.08.002.
Ribeiro, R.P.P.L., Barreto, J., Grosso Xavier, M.D., Martins, D., Esteves, I.A.A.C., Branco, M., Tirolien, T., Mota, J.P.B., Bonfait, G., 2020. Cryogenic neon adsorption on Co3(ndc)3(dabco) metal-organic framework. Microporous Mesoporous Mater. 298. https://doi.org/10.1016/j.micromeso.2020.110055.
Ribeiro, R.P.P.L., Camacho, B.C.R., Lyubchyk, A., Esteves, I.A.A.C., Cruz, F.J.A.L., Mota, J.P.B., 2016. Experimental and computational study of ethane and ethylene adsorption in the MIL-53(Al) metal organic framework. Microporous Mesoporous Mater. 230, 154–165. https://doi.org/10.1016/j.micromeso.2016.05.006.
Ribeiro, R.P.P.L., Sosa, J.E., Araújo, J.M.M., Pereiro, A.B., Mota, J.P.B., 2023. Vacuum swing adsorption for R-32 recovery from R-410A refrigerant blend. Int. J. Refrig. 150, 253–264. https://doi.org/10.1016/j.ijrefrig.2023.01.020.
Rupam, T.H., Islam, M.A, Pal, A., Chakraborty, A., Saha, B.B., 2019. Thermodynamic property surfaces for various adsorbent/adsorbate pairs for cooling applications. Int. J. Heat. Mass Transf. 144, 118579. https://doi.org/10.1016/j.ijheatmasstransfer.2019.118579.
Rupam, T.H., Steenhaut, T., Palash, M.L., Filinchuk, Y., Hermans, S., Saha, B.B., 2022. Thermochemical energy applications of green transition metal doped MIL–100(Fe). Chem. Eng. J. 448, 137590. https://doi.org/10.1016/j.cej.2022.137590.
Russell, S.J., Vines, C.D., Bohrer, G., Johnson, D.R., Villa, J.A., Heltzel, R., Rey-Sanchez, C., Matthes, J.H., 2020. Quantifying CH4 concentration spikes above baseline and attributing CH4 sources to hydraulic fracturing activities by continuous monitoring at an off-site tower. Atmos. Env. 228, 117452. https://doi.org/10.1016/j.atmosenv.2020.117452.
Ruthven, D.M., Lee, L.-K., Yucel, H., 1980. Kinetics of non-isothermal sorption in molecular sieve crystals. AIChE J. 26, 16–23. https://doi.org/10.1002/aic.690260104.
Ryckebosch, E., Drouillon, M., Vervaeren, H., 2011. Techniques for transformation of biogas to biomethane. BioMass BioEnergy 35, 1633–1645. https://doi.org/10.1016/j.biombioe.2011.02.033.
Safa Gamal, M., Asikin-Mijan, N., Arumugam, M., Rashid, U., Taufiq-Yap, Y.H., 2019. Solvent-free catalytic deoxygenation of palm fatty acid distillate over cobalt and manganese supported on activated carbon originating from waste coconut shell. J. Anal. Appl. Pyrolysis. 144, 104690. https://doi.org/10.1016/j.jaap.2019.104690.
Sanchez-Sanchez, M., de Asua, I., Ruano, D., Diaz, K., 2015. Direct synthesis, structural features, and enhanced catalytic activity of the Basolite F300-like semiamorphous

Fe-BTC framework. Cryst. Growth Des. 15, 4498–4506. https://doi.org/10.1021/acs.cgd.5b00755.
Sapnik, A.F., Ashling, C.W., Macreadie, L.K., Lee, S.J., Johnson, T., Telfer, S.G., Bennett, T.D., 2021. Gas adsorption in the topologically disordered Fe-BTC framework. J. Mater. Chem. Mater. 9, 27019–27027. https://doi.org/10.1039/D1TA08449F.
Sayari, A., Belmabkhout, Y., Serna-Guerrero, R., 2011. Flue gas treatment via CO2 adsorption. Chem. Eng. J. 171, 760–774. https://doi.org/10.1016/j.cej.2011.02.007.
Schulz, M., Kourkoulas, D., 2014. Regulation (EU) No 517/2014 of the European Parliament and of the Council of 16 April 2014 on fluorinated greenhouse gases and repealing Regulation (EC) No 842/2006. Off. J. Eur. Union 2014. L150/195-230.
Serafin, J., Dziejarski, B., 2024. Activated carbons—preparation, characterization and their application in CO2 capture: a review. Environ. Sci. Pollut. Res. 31, 40008–40062. https://doi.org/10.1007/s11356-023-28023-9.
Shen, J., Wang, X., Chen, Y., 2023. Adsorbents for adsorption separation of CO2 and CH4: a literature review. Can. J. Chem. Eng. 101, 7115–7133. https://doi.org/10.1002/cjce.24942.
Shen, W., Ma, T., Zuo, L., Yang, X., Cai, J., 2024. Advances and prospects of supercritical CO2 for shale gas extraction and geological sequestration in gas shale reservoirs. Energy Fuels. 38, 789–805. https://doi.org/10.1021/acs.energyfuels.3c03843.
Sing, K.S.W., 1985. Reporting physisorption data for gas/solid systems with special reference to the determination of surface area and porosity (Recommendations 1984). Pure Appl. Chem. 57, 603–619. https://doi.org/10.1351/pac198557040603.
Solomon, K.R., Velders, G.J.M., Wilson, S.R., Madronich, S., Longstreth, J., Aucamp, P.J., Bornman, J.F., 2016. Sources, fates, toxicity, and risks of trifluoroacetic acid and its salts: relevance to substances regulated under the Montreal and Kyoto Protocols. J. Toxicol. Env. Health B Crit. Rev. 19, 289–304. https://doi.org/10.1080/10937404.2016.1175981.
Sosa, J.E., Malheiro, C., Castro, P.J., Ribeiro, R.P.P.L., Piñeiro, M.M., Plantier, F., Mota, J.P.B., Araújo, J.M.M., Pereiro, A.B., 2023. Exploring the potential of metal–organic frameworks for the separation of blends of fluorinated gases with high global warming potential. Glob. Chall. 7, 2200107. https://doi.org/10.1002/gch2.202200107.
Sosa, J.E., Malheiro, C., Ribeiro, R.P.P.L., Castro, P.J., Piñeiro, M.M., Araújo, J.M.M., Plantier, F., Mota, J.P.B., Pereiro, A.B., 2020. Adsorption of fluorinated greenhouse gases on activated carbons: evaluation of their potential for gas separation. J. Chem. Technol. Biotechnol. 95, 1892–1905. https://doi.org/10.1002/jctb.6371.
Sosa, J.E., Ribeiro, R.P.P.L., Castro, P.J., Mota, J.P.B., Pereiro, A.B., Araújo, J.M.M., 2022. Sorption of fluorinated greenhouse gases in silica-supported fluorinated ionic liquids. J. Env. Chem. Eng. 10, 108580. https://doi.org/10.1016/j.jece.2022.108580.
Sosa, J.E., Ribeiro, R.P.P.L., Matos, I., Bernardo, M., Fonseca, I.M., Mota, J.P.B., Araújo, J.M.M., Pereiro, A.B., 2024. Exploring the potential of biomass-derived carbons for the separation of fluorinated gases with high global warming potential. BioMass BioEnergy 188, 107323. https://doi.org/10.1016/j.biombioe.2024.107323.
Staudt, J., Musial, C.M., Canevesi, R., Fierro, V., Ribeiro, C., Alves, H.J., Borba, C.E., 2024. Evaluation of the CH_4/CO_2 separation by adsorption on coconut shell activated carbon: impact of the gas moisture on equilibrium selectivity and adsorption capacity. Heliyon. 10, e30368. https://doi.org/10.1016/j.heliyon.2024.e30368.
Surra, E., Ribeiro, R.P.P.L., Santos, T., Bernardo, M., Mota, J.P.B., Lapa, N., Esteves, I.A. A.C., 2022. Evaluation of activated carbons produced from Maize Cob Waste for adsorption-based CO_2 separation and biogas upgrading. J. Env. Chem. Eng. 10, 107065. https://doi.org/10.1016/j.jece.2021.107065.
Surya Babu, S., Stalinraja, A., Nagasaka, T., Gopalram, K., 2024. Indigenous designed metal-organic framework for electrocatalytic reduction of CO_2—a review. Ion. (Kiel). https://doi.org/10.1007/s11581-024-05468-7.
Tauseef Hassan, S., Danish, A., Baloch, M., Bui, Q., Hashim Khan, N., 2024. The heterogeneous impact of geopolitical risk and environment-related innovations on greenhouse gas emissions: the role of nuclear and renewable energy in the circular economy. Gondwana Res. 127, 144–155. https://doi.org/10.1016/j.gr.2023.08.016.
Thommes, M., Kaneko, K., Neimark, A.V., Olivier, J.P., Rodriguez-Reinoso, F., Rouquerol, J., Sing, K.S.W., 2015. Physisorption of gases, with special reference to the evaluation of surface area and pore size distribution (IUPAC Technical Report). Pure Appl. Chem. 87, 1051–1069. https://doi.org/10.1515/pac-2014-1117.
Vargas, D.P., Giraldo, L., Moreno-Piraján, J.C., 2012. CO2 Adsorption on activated carbon honeycomb-monoliths: a comparison of Langmuir and Tóth models. Int. J. Mol. Sci. 13, 8388–8397. https://doi.org/10.3390/ijms13078388.
Vimont, A., Travert, A., Bazin, P., Lavalley, J.-C., Daturi, M., Serre, C., Férey, G., Bourrelly, S., Llewellyn, P.L., 2007. Evidence of CO2 molecule acting as an electron acceptor on a nanoporous metal–organic-framework MIL-53 or Cr3+(OH)(O2C–C6H4–CO2). Chem. Commun. 3291–3293. https://doi.org/10.1039/B703468G.
Vollmer, M.K., Rhee, T.S., Rigby, M., Hofstetter, D., Hill, M., Schoenenberger, F., Reimann, S., 2015. Modern inhalation anesthetics: potent greenhouse gases in the global atmosphere. Geophys. Res. Lett. 42, 1606–1611. https://doi.org/10.1002/2014GL062785.
Wang, Q., Huang, Z., Ou, S., Zhang, R., 2019. The energy storage properties of refrigerants (R170, R134a, R143a, and R152a) in mof-5 nanoparticles: a molecular simulation approach. Materials 12. https://doi.org/10.3390/ma12213577.
Wang, Z., Wang, Y., Li, J., Henne, S., Zhang, B., Hu, J., Zhang, J., 2018. Impacts of the degradation of 2,3,3,3-tetrafluoropropene into trifluoroacetic acid from its application in automobile air conditioners in China, the United States, and Europe. Env. Sci. Technol. 52, 2819–2826. https://doi.org/10.1021/acs.est.7b05960.
Wanigarathna, D.K.J.A., Gao, J., Liu, B., 2020. Metal organic frameworks for adsorption-based separation of fluorocompounds: a review. Mater. Adv. 1, 310–320. https://doi.org/10.1039/d0ma00083c.
Wanigarathna, D.K.J.A., Gao, J., Liu, B., 2018. Fluorocarbon separation in a thermally robust zirconium carboxylate metal–organic framework. Chem. Asian J. https://doi.org/10.1002/asia.201800337.
Xiang, Z., Peng, X., Cheng, X., Li, X., Cao, D., 2011. CNT@Cu3(BTC)2 and metal–organic frameworks for separation of CO_2/CH_4 mixture. J. Phys. Chem. C 115, 19864–19871. https://doi.org/10.1021/jp206959k.
Yahya, M.A., Mansor, M.H., Zolkarnaini, W.A.A.W., Rusli, N.S., Aminuddin, A., Mohamad, K., Sabhan, F.A.M., Atik, A.A.A., Ozair, L.N., 2018. A brief review on activated carbon derived from agriculture by-product. AIP. Conf. Proc. 1972, 030023. https://doi.org/10.1063/1.5041244.
Zeng, Q.-W., Hu, L., Niu, Y., Wang, D., Kang, Y., Jia, H., Dou, W.-T., Xu, L., 2024. Metal–organic cages for gas adsorption and separation. Chem. Commun. 60, 3469–3483. https://doi.org/10.1039/D3CC05935A.